Non destructive Eddy Currents inversion using Artificial Neural Networks and data augmentation

R. Cormerais, Roberto Longo, A. Duclos, G. Wasselynck, G. Berthiau

Non destructive Eddy Currents inversion using Artificial Neural Networks and data augmentation

R. Cormerais [a,b,c], Roberto Longo [b,c,*], A. Duclos [c], G. Wasselynck [a], G. Berthiau [a]

[a] Institut de Recherche en Énergie Électrique de Nantes Atlantiques (IREENA), 37 Blvd de l'Université, Saint-Nazaire, France
[b] Groupe Signal Image et Instrumentation (GSII), École Supérieure d'Électronique de l'Ouest (ESEO), 10 Blvd Jean Jeanneteau, Angers, France
[c] Laboratoire d'Acoustique de l'Université du Mans (LAUM), UMR 6613, Institut d'Acoustique - Graduate School (IA-GS), CNRS, Le Mans Université, 72085, Le Mans, France

ARTICLE INFO

Keywords:
Eddy currents testing
Artificial neural network
Data augmentation
Principal component analysis

ABSTRACT

Eddy Currents (ECs) for Non Destructive Testing (NDT) is a method to determine the presence of flaws in metal materials. The estimation of flaw parameters like position and size through physical models is usually difficult. This article offers an alternative technique based on machine learning algorithms such as Artificial Neural Networks (ANNs). This approach often requires simulated signals to build an exhaustive training data-set, leading to a considerable amount of calculation time and resources. To deal with this problem, this article proposes a new method based on data augmentation via Principal Component Analysis (PCA). The presented method is evaluated using different kinds of simulated and experimental signals.

1. Introduction

Non Destructive Testing (NDT) is a wide group of analysis techniques employed to asses the quality and to evaluate the safety of materials in building or transport industry [1]. These non invasive methods allow to monitor materials during their manufacturing, assembling and their lifetime. The flaws to be detected can be of different types, sizes and orientations and may be located in a large variety of materials. Various techniques are used in NDT such as Ultrasonic Testing (UT), Eddy Currents (ECs), radiography, penetrant testing and thermography [2,3]. These methods present different advantages on their capabilities to detect flaws of specific shapes, on their implementations and on the nature of the materials that can be tested. Most NDT techniques make use of ECs to determine position and size of structural flaws in metal materials [4–9]. An electromagnetic field is induced into the conductive material under investigation, creating an ECs flow propagating into the structure. Variations on the coil impedance are monitored to detect and characterize defects eventually present [10]. However, the skin effect limits the use of ECs in cases where flaws are located very close to the surface of the inspected parts. UT is another NDT method widely used in a large variety of materials. Mechanical waves traveling through the inspected parts are reflected by flaws present. However the blind zone called near field of UT makes it unsuitable for detecting surface of sub-surface flaws without using specific coupling techniques (i.e. wedges).

Hence, this article represents a first step for a future combined use of ECs and UT. It focuses on the ECs part, while the combination with ultrasonic inspection is still object of current study.

Generally speaking, the state of the art related to ECs testing considers complex physical modeling leading to difficult estimations of flaw parameters like length and depth [11]. Some works analytically solve this inversion problem under particular conditions as surface cracks or specific geometries [12,13]. An analytic algorithm for defect shape reconstruction using multi-coil measurement system is also presented in Ref. [14]. Other approaches make use of surrogate models [15], in which look-up tables are composed by experimental measurements and/or numerical simulations. New measurement data are subsequently treated via regression or interpolation algorithms [16–19].

During the last decade, Machine Learning (ML) approaches making use of ECs measurements have been employed to estimate flaws parameters such as depth and length. Algorithms based on Support Vector Machines (SVMs) registered good performances if applied to data-sets of a reduced size, making use of under-constraints optimization routines to reach the global minimum [20–25].

Other studies focus instead on Artificial Neural Networks (ANNs) [26–33], as they can theoretically learn any function as long as one can

* Corresponding author. École Supérieure d'Électronique de l'Ouest (ESEO), 10 Blvd Jean Jeanneteau, 49107, Angers, France.
E-mail address: roberto.longo@eseo.fr (R. Longo).

provide enough data [34–36]. To improve the ANNs generalization performances, a feature extraction approach has been proposed in Ref. [37].

In this paper an ML approach based on ANN will be presented. The main reason behind this choice is to exploit the ANN flexibility for future integration with UT data. Due to the difficulties often encountered on building an exhaustive experimental data-set to train the ANN, measurements have been replaced by numerical simulations. The main disadvantage in using simulated data is represented by the significant computing time and resources needed to build an exhaustive training data-base [38]. This drawback has been overcome in Refs. [21,23,39], by computing only the minimal number of well-chosen training sample by means of space filling algorithms [40], i.e. Latin Hypercube Sampling [39]. However, these methods still need a grid sampling as starting point and to validate the final results.

This article presents a new approach based on data augmentation algorithms via Principal Component Analysis (PCA). The aim is to provide an exhaustive training data-base, together with a significant reduction of computing time and resources. All simulations are adapted to an Aluminum block using a Finite Element Method (FEM) which refers to the electric vector potential and magnetic scalar potential T − Ω formulation [41,42], as briefly reported in Section 2.1. The data augmentation algorithm is implemented via 3D interpolations over the principal components, as described in Section 2.2. The simulated original data-set, the PCA compressed data and the augmented ones are employed to train the ANN described in Section 3. The main results are reported in the same section. Measurements are then performed on an Aluminum block providing a first experimental validation (see Section 4.1). Final results are reported in Section 4.2 proving that an ANN is able to estimate Side Drill Holes (SDHs) parameters (radius and depth) and that the data augmentation allows the use of a reduced training set without deteriorating the flaws parameters estimations.

2. Simulated data-base for non destructive Eddy Currents testing

2.1. Finite elements method in presence of Side Drill Holes

In this section, signals from homogeneous Aluminum blocks containing SDHs are obtained via the electric vector potential and magnetic scalar potential $\vec{T} - \Omega$ FEM formulation adapted to multi-connected geometries [42]. This formulation allows reduction of simulation time by computing electric vector potential only in the conductive domain. The coil supply is sinusoidal, which allows the study in the harmonic regime. The magnetic field $\vec{H}$ is expressed through a magnetic source field $\vec{H_S}$ and an electric potential vector $\vec{T}$ such that $\vec{J_{ind}} = \vec{\nabla} \times \vec{T}$ in the conductive domain and $\vec{T} = \vec{0}$ outside. $\vec{H}$ and $\vec{T}$ are linked by $\vec{H} = \vec{H_S} + \vec{T} - \overrightarrow{\text{grad}}\,(\Omega)$ where Ω is the magnetic scalar potential. To obtain a unique solution and because magnetic potential varies from zero to infinity, $\Omega = 0$ is imposed on the surface of an air box surrounding the simulated domain. Moreover, $\vec{T}$ is set to $\vec{0}$ on the conductive domain surface. An implicit gauge condition through an iterative resolution algorithm allows convergence and uniqueness of the solution. The electrical conductivity and magnetic relative permeability are defined as $\sigma = 37.7$ MS m^{-1} and $\mu_r = 1$. These calculations allow to compute the induced currents $\vec{J}$, the electric field $\vec{E}$, the magnetic induction $\vec{B}$ and the magnetic field $\vec{H}$. The active and reactive impedance R and X of the simulated probe are derived from the active dissipated power in the conductive domain D_c and the reactive dissipated power in the simulated domain D following Eq. (1) and Eq. (2). This allows computation of the impedance variation of the inductor due to the presence of the flaw. In order to avoid the meshing of the coil, the reaction of the probe to the electro-magnetic field generated by ECs has not been taken into account during the simulation phase.

An 'in house' data-set of 3000 different cases is built, varying the

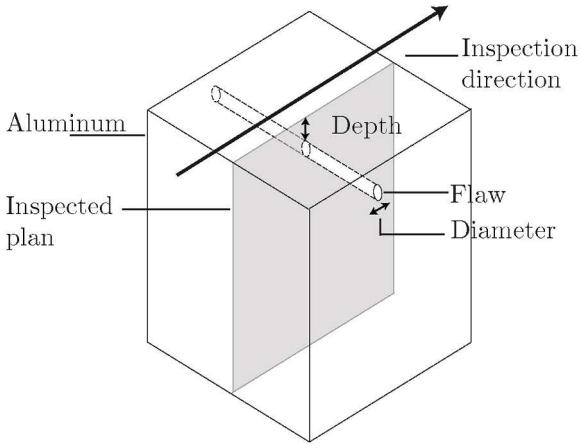

Fig. 1. Simulated Aluminum block containing a Side Drill Hole (SDH).

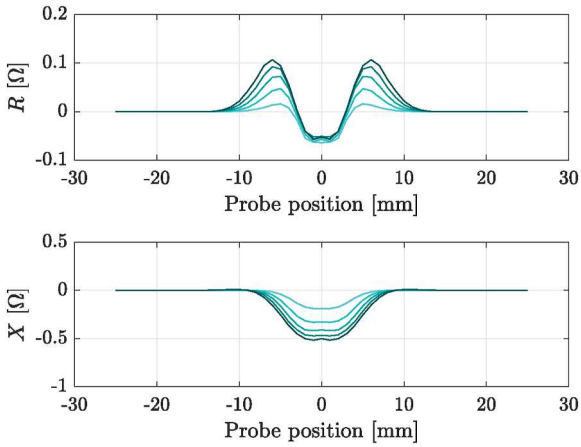

Fig. 2. Active R and reactive X impedance variations obtained simulating SDHs, with radius from 1 (cyan) to 5 mm (black) at a depth of 1 mm. (For interpretation of the references to colour in this figure legend, the reader is referred to the Web version of this article.)

parameters of cylindrical flaws from a radius of 0.6–8 mm and from a depth of 0.1–4 mm (see Fig. 1), depth being the distance between the surface and the top of each flaw. A nonlinear least-squares optimization [43] between simulations and experimental signals (Section 4.1) is implemented to estimate the probe parameters, leading to an ECs coil composed by a 2.25 mm height and 1400 windings with inner and outer radius of 2.22 and 2.48 mm driven by a sinusoidal signal at 1 kHz. Air gap is set to 0.18 mm. The skin depth δ, defined by Eq. (3), is equal to 2.59 mm, consequently no SDH is expected to be detected after 7 mm depth, corresponding to 3δ. The probe response is simulated every millimeter along the inspection direction (see Fig. 1). A workstation equipped with an Intel I7 Processor, an NVIDIA Quadro P3000 Graphic Computing Units (GPUs) and 16 Gb of RAM has been employed to produce the data-set, requiring a calculation time of approximately 2000 h. The data augmentation method proposed in Section 2.3 will artificially replace some portions of this original data set, according to a decimation factor. The ANN performances will be than compared to the ones obtained with the complete data-set and the decimated one. Examples of simulated signals interacting with SDHs from 1 to 5 mm radius and located at 1 mm depth under the inspected surface are depicted in Fig. 2. The ECs signals show symmetrical properties. These symmetries imply redundancy in the training data, which could protract the ANN training time. For these reasons, input data need to be pre-processed in order to discriminate useful information. To do so, a method based on PCA will be presented in the next paragraph.

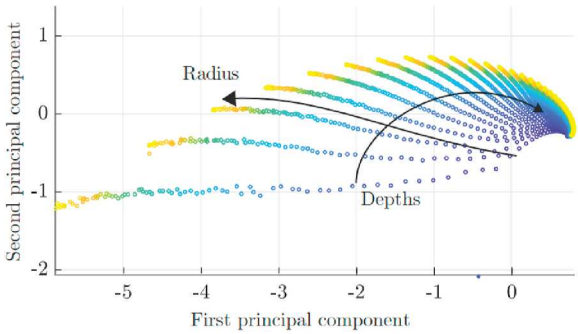

Fig. 3. Simulated flaws radius and depths represented as a function of the two first principal components. Radius varies from 0.6 (blue) to 8 mm (yellow) and depth from 0.1 to 4 mm. (For interpretation of the references to colour in this figure legend, the reader is referred to the Web version of this article.)

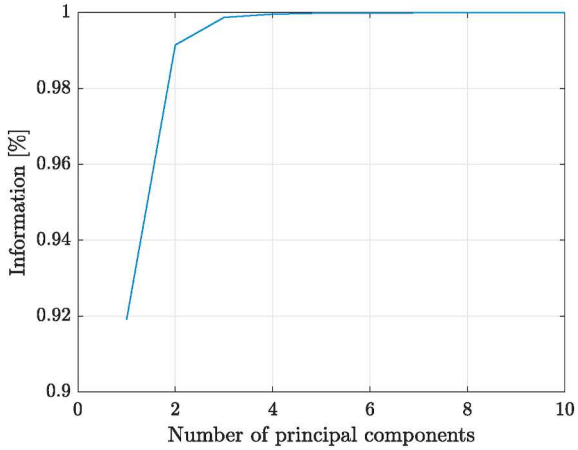

Fig. 4. Normalized cumulative sum of the first ten eigenvalues. The two first PCs have captured 99% of the information from the original data.

$$RI^2_{source} = \int_{D_c} \vec{E}\cdot\vec{J}\,dD_c = \int_{D_c} \sigma^{-1}\vec{J}\cdot\vec{J}\,dD_c, \tag{1}$$

$$jXI^2_{source} = \int_D \frac{\partial \vec{B}}{\partial t}\cdot\vec{H}\,dD = j\omega\int_D \mu^{-1}\vec{B}\cdot\vec{B}\,dD, \tag{2}$$

$$\delta = \frac{1}{\sqrt{\pi\mu\sigma f}}. \tag{3}$$

2.2. Principal Component Analysis

By definition, PCA is a statistical method that uses an orthogonal transformation to express potentially correlated observations into linearly uncorrelated variables called Principal Components (PCs). This transformation is defined in a way that the first PC presents the largest possible variance, and each succeeding component in turn has the highest variance possible in the orthogonal basis [44]. Some work successfully processed ECs signals with the use of PCA [28,45]. By selecting specific PCs, it is possible to compress the original data by avoiding redundancy that is present. As example, Fig. 3 depicts the radius (top graph) and depth (bottom graph) evolution in function of the two fist PCs. A common way to choose the minimum number of PCs needed to correctly represent the original data is to look at the cumulative sum of eigenvalues. For illustration purposes, the cumulative sum of the first ten eigenvalues is plotted in Fig. 4, indicating that 99% of PCA space information is concentrated in the first two components.

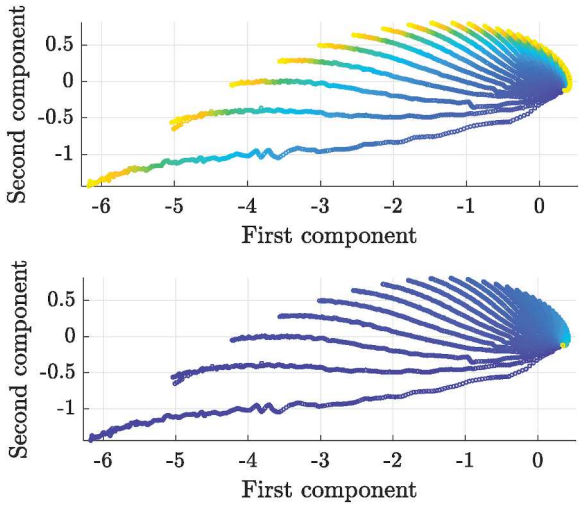

Fig. 5. Augmented data for flaws radius (top graph) and depths (bottom graph) represented in function of the two principal components. Radius varies from 0.6 (blue) to 8 mm (yellow) and depth from 0.1 (blue) to 4 mm (yellow). (For interpretation of the references to colour in this figure legend, the reader is referred to the Web version of this article.)

2.3. Data augmentation procedure

This section presents the data augmentation method used to process simulated signals. This approach relies on PCA method, mentioned in the previous paragraph. Indeed, from the PCA representation, additional artificial data at given depth and radius can be inserted in the PCA space.

In example, for the case of the first PCs, artificial data are inserted computing cubic spline interpolations [46]. More in detail, if r_1 and r_2 represent two simulated radius at a given depth, we indicate their corresponding first PCs as $PC_1(r = r_1)$ and $PC_1(r = r_2)$. The slope of the curve $PC_1(r)$ is instead labeled as t_1 for $r = r_1$ and t_2 for $r = r_2$, as reported in Eq. (4). The first interpolated PC at a given radius between r_1 and r_2 is given by $PC_1^{interp}(r)$ in Eq. (5) where p_0, p_1, p_2 and p_3 are defined in Eq. (6). Subsequently, the augmented second PCs for the new artificial radius values, here called $PC_2^{interp}(r)$, are calculated through linear two dimensional Delaunay triangulation interpolations [47]. It can be shown that this will result in a $PC_2^{interp}(r)$ being function of $PC_1^{interp}(r)$, $PC_1(r = r_1)$, $PC_1(r = r_2)$, $PC_2(r = r_1)$, $PC_2(r = r_2)$ and $PC_1^{interp}(r)$. The entire mathematical formulation for $PC_2^{interp}(r)$ will not be reported here. We refer to Ref. [47] for additional details.

To sum-up, Fig. 5 depicts the new data-set artificially augmented by a factor of five. This means that five artificial points have been added for every simulated point, corresponding to five new radii at each simulated depth.

In the next section the ANN estimations will be presented, offering a comparison between the different training procedures composed by the original simulated data-set and the artificial one.

$$\begin{cases} PC_1 = PC_1(r = r_1), & \dfrac{dPC_1}{dr} = t_1 \quad \text{at} \quad r = r_1, \\ PC_1 = PC_1(r = r_2), & \dfrac{dPC_1}{dr} = t_2 \quad \text{at} \quad r = r_2. \end{cases} \tag{4}$$

$$PC_1^{interp}(r) = p_0 + p_1(r - r_1) + p_2(r - r_1)^2 + p_3(r - r_1)^3. \tag{5}$$

$$
\begin{aligned}
&p_0 = PC_1(r = r_1),\\
&p_1 = t_1^{'},\\
&\{p_2 = \frac{3\dfrac{PC_1(r = r_2) - PC_1(r - r_1)}{r_2 - r_1}}{r_2 - r_1},\\
&p_3 = \frac{t_1 + t_2 - 2\dfrac{PC_1(r = r_2) - PC_1(r = r_1)}{r_2 - r_1}}{(r_2 - r_1)^2}.
\end{aligned}
\tag{6}
$$

3. Artificial neural network training and preliminary results

Artificial Neural Networks (ANNs) are employed in this work to estimate flaws parameters from ECs signals, offering an alternative to inversion algorithms based on physical models. Generally speaking, an ANN is composed of simple interconnected computing units trained to fit relations between data. An algorithm based on error back-propagation is implemented to find the weights firstly randomly initialized. The goal is to minimize the chosen error function between the network outputs and the desired ones over the training samples [34]. Eventually, the Mean Squared Error (MSE) is calculated to evaluate the ANN performances [48]. As the weights are randomly initialized, each training procedure can lead to different results. For this reason, ANNs are often trained several times in order to get the mean value of the different results that ware obtained. The ANN presented in this study was implemented making use of Matlab Statistics and Machine Learning Toolbox. The architecture is composed by two inputs corresponding to two features extracted from ECs signals. Firstly, the two inputs of the ANN are chosen as the maximum of the complex impedance of each defect, i.e. the simulated signals for a probe position of zero millimeter. Secondly, the two first principal components are used as inputs as they contain most of the information from the simulated signals. The ANN inputs are connected to an hidden layer of 20 neurons. This value, being set empirically, assures accurate estimations without risking over-fitting. The final layer is composed of two outputs neurons representing the radius and depths estimations. The activation functions are chosen to form an universal function estimator [34,36].

In order to evaluate the estimation errors of the ANN simulated data are split into training data-set (50%), validation data-set (25%) and test data-set (25%), as proposed in Refs. [35,36]. Validation and test samples are evenly distributed to assess performances of the ANN all over the flaw parameters space. The PCA presented in the previous section is then employed for the training data-base. Validation and test data-set are subsequently projected in the created PCs space. Same procedure will be followed for the experimental measurements presented in Section 4. Training samples are used by the training algorithm to update the weights of the network at every iteration, called epoch. In order to obtain an ANN with good generalization performances, the validation samples are employed to implement an early stopping strategy. The training algorithm monitors validation error and stops when prediction performances begin to decrease. The test samples are not used during training and are considered as new measurements allowing to measure the estimation errors of the ANNs in presence of unknown data.

We now focus our attention in the optimization procedure employed to find the best values for the ANN weights during the ANN training. In detail, we refer to the Levenberg-Marquardt back-propagation algorithm [35,49], where the optimal values W which minimize the overall quadratic error E of the training data-set are calculated iteratively. Hence, starting from initial conditions randomly chosen, the weights W_{k+1} at the $k+1$ iteration are computed following Eq. (7). The update parameter ΔW is defined in Eq. (8). The matrix J appearing in Eq. (8) represents the Jacobian matrix computed through back-propagation, while e indicates the error vector between actual and desired output.

The advantage of this method is the introduction of the parameter μ in Eq. (8). This can be considered an adaptive learning rate which

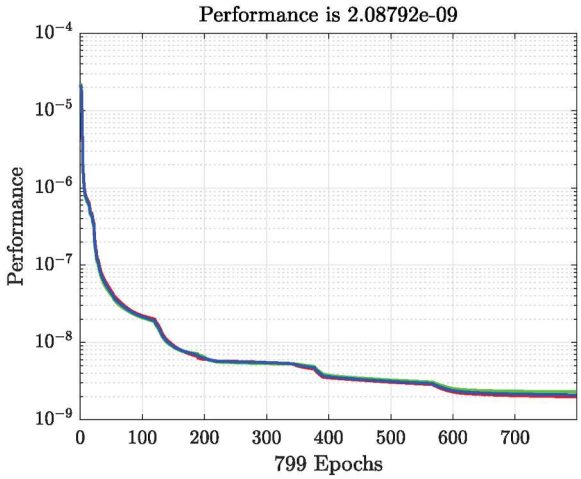

Fig. 6. Train (blue), validation (green) and test (red) ANN performances in function of the number of epochs for a training example, with β_{dec} and β_{inc} respectively set to 0.1 and 10. (For interpretation of the references to colour in this figure legend, the reader is referred to the Web version of this article.)

provides an automatic trade-off between guaranteed algorithm convergence and speed. With high values of μ, Eq. (8) becomes similar to the steepest descent, with descent speed modulated by $\frac{1}{\mu}$. On the other hand, when μ is small Eq. (8) approximates the Gauss-Newton method [49]. To sum-up the, the ANN weights optimization follows the steps indicated below:

1. Compute the ANN output for each training samples and the actual overall quadratic error E.
2. Compute the Jacobian matrix.
3. Compute the weights update using Eq. (8).
4. Compute the variation of the overall quadratic error ΔE with the updated weights $W + \Delta W$:
   - if $\Delta E < 0$ μ, is multiplied by a reduction factor β_{dec} and the algorithm goes back to step 1.
   - if $\Delta E > 0$ μ, is multiplied by an increasing factor β_{inc} and the algorithm goes back to step 3.
5. The algorithm stops when the quadratic error over the validation data-set increases for more than 10 epochs.

$$W_{k+1} = W_k + \Delta W \tag{7}$$

$$\Delta W = [J^T(W)J(W) + \mu I]^{-1} J^T(W)e(W) \tag{8}$$

As staring point, the initial value for μ has been set to 0.001. Values for β_{dec} and β_{inc} have been set empirically to 0.1 and 10 respectively. It is worthy to mention that values of β_{dec} and β_{inc} close to 1 lead to an optimization procedure characterized by a slow convergence and consequently it implies a considerable amount of epochs. Values much greater than 1 could make the algorithm converge to a local minimum. The evolution of the MSE over each data-set during a training example is plotted in Fig. 6. As expected, the training error MSE decreases over training samples. The validation and test error closely follow the training one, showing a good generalization. Eventually, the training stops at 799 epochs because the validation MSE did not change over the last ten epochs.

In the next paragraph, different training strategies will be presented, using as ANN inputs the simulated impedance at the center of flaws and the two first PCs, alternatively. Eventually, the proposed data augmentation will be evaluated by progressively decimating the training data-set and by replacing the missing points with artificial ones following the procedure mentioned in Section 2.2.

No scaling have been applied to raw data as they already vary in the range [-1 1], nor to PCs as they are scaled by construction.

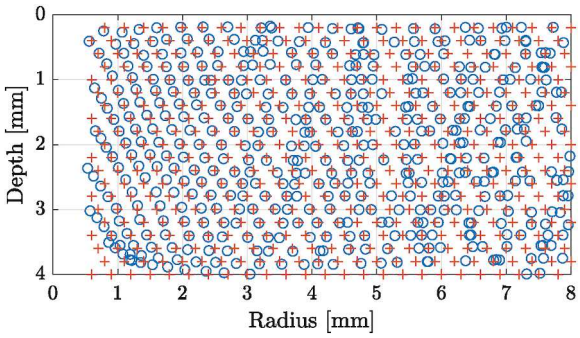

Fig. 7. ANN depths and radius estimations (circles) compared to actual parameters (crosses) over the test data-set **using complex impedance as inputs** of the ANN. The corresponding RMSE registered the value of 0.09 mm.

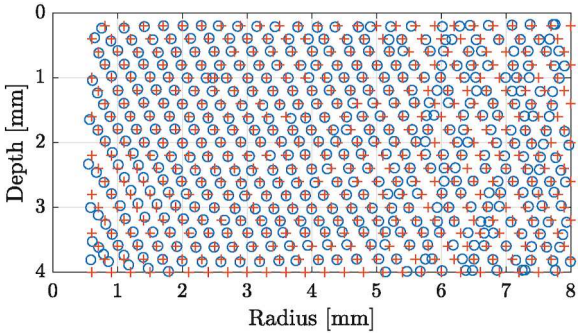

Fig. 8. ANN depths and radius estimations (circles) compared to actual parameters (crosses) over the test data-set **using principal components as inputs** of the ANN. The corresponding RMSE registered the value of 0.03 mm.

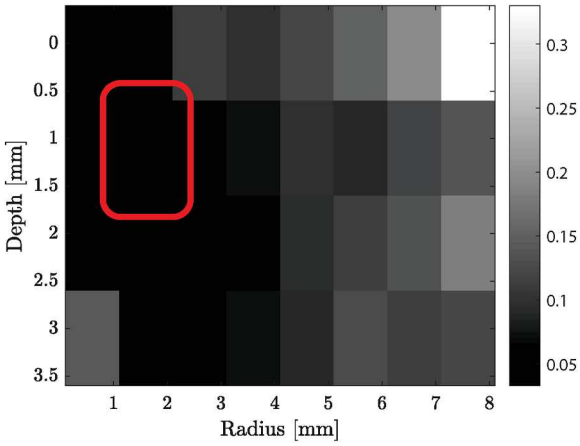

Fig. 9. Absolute error map of the radius estimations as a function of the actual depths and radius **using complex impedance values as inputs** of the ANN. For a flaw with a radius between 1 and 2 mm located at a depth between 0.5 and 1.5 mm (continuous box), the radius mean absolute error estimation is 0.05 mm.

3.1. Artificial neural network results with simulated data

This section presents the radius and depths estimations obtained using three different strategies. First, the ANN is trained and tested using complex impedance from the original data-set (i.e. the 3000 cases reported in Section 2.1). Fig. 7 shows the comparison between ANN estimations and actual values over the test data-set. These estimations present a Root Mean Square Error (RMSE) of 0.09 mm. The estimations

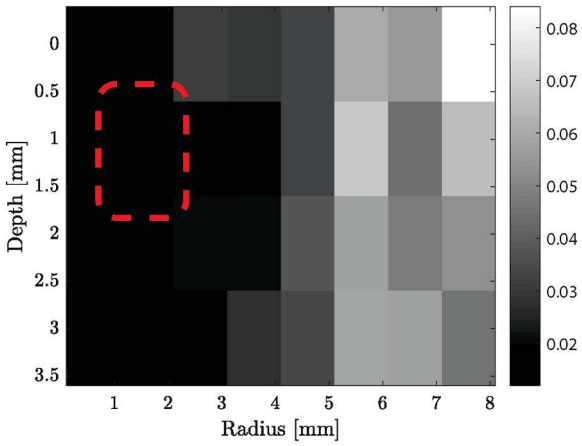

Fig. 10. Absolute error map of the radius estimations as a function of the actual depths and radius **using principal components as inputs** of the ANN. For a flaw with a radius between 1 and 2 mm located at a depth between 0.5 and 1.5 mm (dotted box), the radius mean absolute error estimation is 0.01 mm.

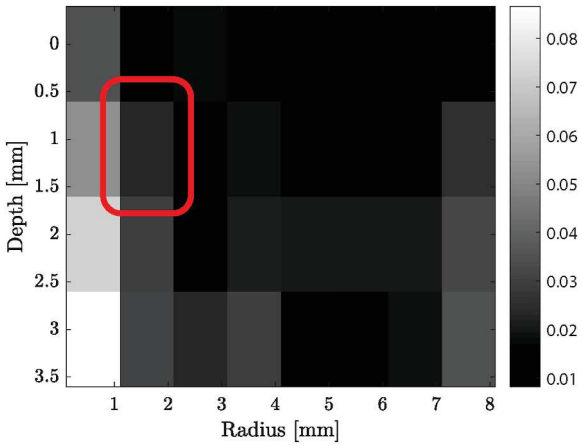

Fig. 11. Absolute error map of the depths estimations as a function of the actual depths and radius **using complex impedance values as inputs** of the ANN. For a flaw with a radius between 1 and 2 mm located at a depth between 0.5 and 1.5 mm (continuous box), the depth mean absolute error estimation is 0.02 mm.

are expected to be less accurate as the radius of SDHs become larger than the probe. The mean absolute error for radius and depths estimations are respectively averaged by zones in Fig. 9 and Fig. 11. The radius absolute estimation error varies from 0.032 to 0.33 mm and the depth absolute estimation error from 0.0082 to 0.087 mm. For example, a given flaw with an estimated radius of 2 mm located at an estimated depth of 1 mm (continuous boxes in Figs. 9 and 11) presents a mean absolute error of 0.05 and 0.02 mm for the radius and depth respectively.

Secondly, the ANN is trained and tested using the two first principal components. Fig. 8 compares ANN estimations over the test data-set versus actual values. The RMSE is decreased by a factor of three, reaching 0.03 mm. The estimations are improved even for large radius. Figs. 10 and 12 respectively present the radius and depth mean absolute estimations errors by zones. These errors vary from 0.012 to 0.084 mm for the radius and from 0.0051 to 0.062 mm for the depth. For example, a given flaw with a radius of 2 mm located at a depth of 1 mm (dotted boxes in Figs. 10 and 12) shows a mean absolute error of 0.01 mm for the radius and 0.008 mm for the depth. The first important conclusion is that PCA gives the possibility to reduce the estimation errors, in particular for the radius.

To examine the effect of decimation and augmentation further pairs

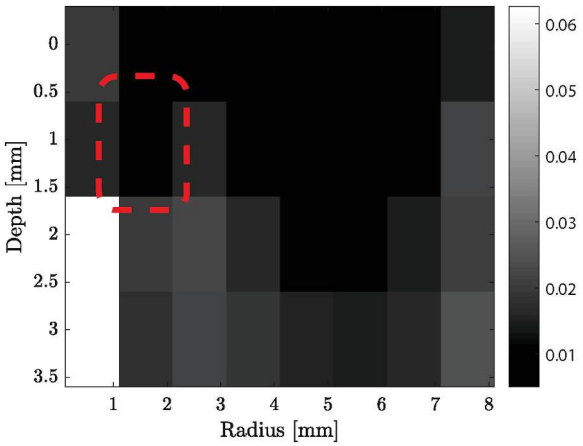

Fig. 12. Absolute error map of the depths estimations as a function of the actual depths and radius **using principal components as inputs** of the ANN. For a flaw with a radius between 1 and 2 mm located at a depth between 0.5 and 1.5 mm (dotted box), the depth mean absolute error estimation is 0.008 mm.

of ANNs were trained. In one (decimated), the training data was decimated by a given factor (0 = no decimation, 10 = reduced by a factor of 10). In the complimentary ANN (augmented), the decimated data was replaced by interpolated (augmented) data to bring the size of the training set back up to the original size. For example, a factor of five leads to take into account for the training procedure only one point every five simulated ones, with the direct consequence of dividing the simulation time by the same factor. The removed samples are replaced using the proposed data augmentation algorithm. Radius and depths estimations accuracy is monitored through the relative MSE over the original test data-set. Fig. 13 compares the MSE obtained decimating and augmenting the training data-set as function of the decimated factor. Using the decimated data-set, an average error of 1000% is recorded for a decimation factor of eight. This high error value was expected as the ANN is trained with a reduced data-set and tested on the original test data. The best performance was reached at the error of 46%. In comparison, an average error of 9% and a minimum error of 6% are recorded for the same decimation factor using the data augmentation to replace decimated samples. In conclusion, despite a number of actual simulations divided by a factor of eight, the proposed method allows to greatly reduce the estimations MSE. Moreover, it needed only 250 h of calculation time instead of the 2000 h necessary to build the original database. In addition, this method also reduced the variability of ANN performances avoiding the need for a large number of training. Taking into account these preliminary results a first experimental validation to this approach is presented in the next section, with the aim to evaluate the entire procedure when using experimental data.

4. Experimental validation

4.1. Experimental set-up for Eddy Currents evaluation

In order to validate the proposed approach, ECs signals are measured over an Aluminum test sample containing two SDHs. The two flaws present a radius of 2.5 mm and are located at depths of 1 and 3 mm as depicted in Fig. 14. The experimental setup consists of a NORTEC 600 flaw detector with a low frequency probe provided by Olympus. Care was taken to configure the experimental set-up as close as possible to the simulations parameters detailed in Section 2.1. The measuring device induces an electromagnetic field at the frequency of 1 kHz and monitors the impedance variations. The electrical conductivity and magnetic relative permeability are considered as equal to $\sigma = 37.7$ MS m^{-1} and $\mu_r = 1$, leading to a skin depth δ of approximately 2.5 mm as reported in Eq. (3). We empirically set the optimal angle between the probe and the surface under test, monitoring the signal amplitude recorded during repeated measurements. The probe is moved by a step motor along the inspected surface. The active (R) and reactive (X) impedances are measured every millimeter. The measured signals and the corresponding simulated ones are compared in Fig. 15. Signals from the first flaw (see Fig. 15 (a)) located at a depth of 1 mm are close to the corresponding simulated ones, offering a validating to the numerical procedure. Signals from the second flaw Fig. 15 (b) at a depth of 3 mm are slightly different compared to the simulated reactive impedance. This difference is due to the fact that the simulations of Section 2 did not take into account the reaction of the probe to the field generated by ECs [42], as already

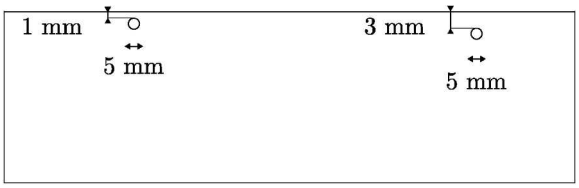

Fig. 14. Scheme of the experimental sample containing two SDHs with radius of 2.5 mm and located at depths of 1 and 3 mm.

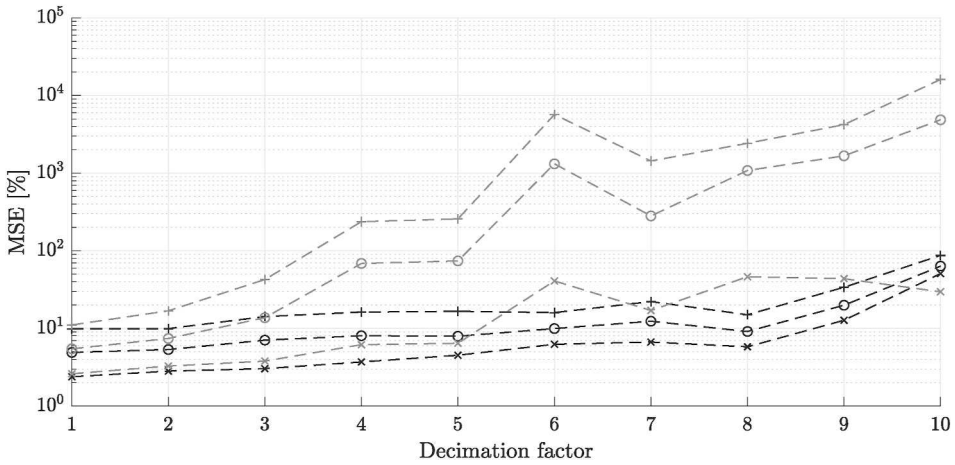

Fig. 13. Maximum (+), mean (o) and minimum (x) MSEs obtained decimating the training data-set (grey) and using the data augmentation procedure (black). For a decimation factor of eight, the radius and depths estimations present an average error of 9%, within a minimum value of 6% and a maximum of 15% using data augmentation against an average error of 1000%, within a minimum value of 46% and a maximum of 2400% when only decimating the training data.

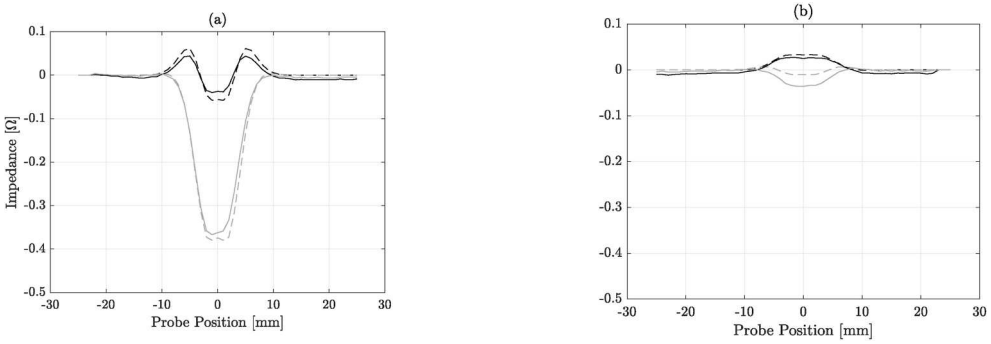

Fig. 15. Experimental (−) and simulated (−−) active R (black) and reactive X (grey) impedance from SDHs with radius of 2.5 mm located at depths of 1 (a) and 3 mm (b).

Table 1
Radius and depths estimations [mm] obtained analyzing measured signals from **the first flaw** using the ANN trained with different inputs.

Flaw 1	Radius	Depth
True values	2.5	1
Original data-set estimation	2.61 ± 0.05	1.06 ± 0.02
Principal components estimation	2.38 ± 0.03	1.03 ± 0.02
Data augmentation estimation	2.36 ± 0.03	1.03 ± 0.01

Table 2
Radius and depths estimations [mm] obtained analyzing measured signals from **the second flaw** using the three different inputs.

Flaw 2	Radius	Depth
True values	2.5	3
Original data-set estimation	1.23 ± 0.05	2.25 ± 0.02
Principal components Estimation	1.27 ± 0.03	2.25 ± 0.02
Data augmentation Estimation	1.22 ± 0.08	2.24 ± 0.03

mentioned in Section 2.1.

4.2. Results and discussions

This paragraph presents the radius and depths estimations obtained with measured signals using the ANN trained firstly with complex impedance from simulated data-set, secondly with the two first principal components and eventually with the proposed data augmentation procedure. The radius and depths estimations given by the ANN using the three types of inputs as training data are respectively reported in Table 1 and Table 2 for the first and second flaw. The first SDH with a radius of 2.5 mm and located at a depth of 1 mm is estimated with radius of 2.61, 2.38 and 2.36 mm and at estimated depths of 1.06, 1.03 and 1.03 mm (Table 1), using original data, principal components and augmented data respectively. These results show that the ANN can estimate the flaw parameters relatively accurately in each training case. The second flaw with a radius of 2.5 mm and located at a depth of 3 mm is estimated with radius of 1.23, 1.27 and 1.22 mm and at depths of 2.25, 2.25 and 2.24 mm (Table 2), respectively, using the three types of inputs. These estimation errors are explained by the differences between simulations and measurements observed in Fig. 15 (b). For the first flaw, the simulated signal which better represented the experimental one presented a radius of 2.36 mm and was located at the depth of 1.03 mm (see. Fig. 16 (a)), explaining the values reported in Table 1. For the second flaw, the best match between simulated and measured signal was reached at the depth of 2.24 mm and a radius of 1.22 mm (see. Fig. 16 (b)). This explains the difficulties to properly estimate the real flaw parameters, especially the radius as highlighted in Table 2. It is also important to point out that, even in the experimental case, the proposed data augmentation method helps achieve better accuracy and precision, despite the fact that the number of simulated samples is divided by eight.

5. Conclusion

Artificial Neural Networks are a promising tool for Eddy Currents testing as they offer an alternative way for flaw parameters estimations. Nowadays, the main drawback of this method still resides on the large amount of training data. To overcome this limitation, a data augmentation method based on Principal Component Analysis and 3D interpolation has been presented in this article. The proposed procedure was adapted to Side Drill Holes.

More complex flaw geometries may require different linear or non-linear transformations of the input data.

First results using simulated data showed that this procedure allowed

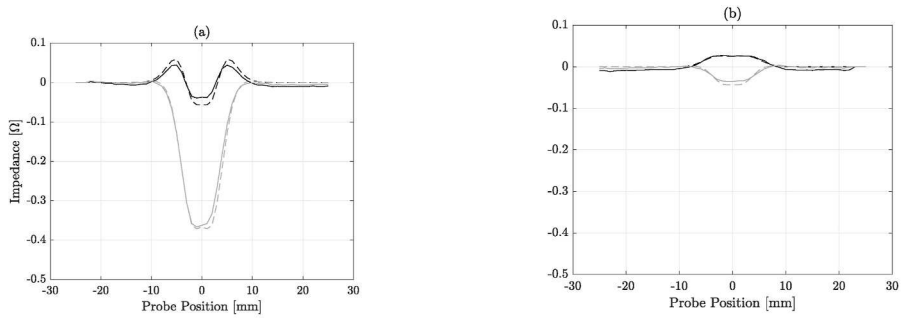

(a) Experimental (−) ECs signals from SDHs with radius of 2.5 mm located at depths of 1 and simulated (−−) signals from SDHs with a radius of 2.36 mm located at a depth of 1.03 mm.

(b) Experimental (−) ECs signals from SDHs with radius of 2.5 mm located at depths of 3 mm and simulated (−−) signals from SDHs with a radius of 1.22 mm located at a depth of 2.24 mm.

Fig. 16. Simulated signals which better represent the experimental ones. Active impedance R is traced in black and reactive one X in grey.

to reduce the number of samples by analytically completing a sparse data-base. Eventually, the ANN has been implemented to process experimental data. Due to some limitations concerning the FEM model used to compute the training data-set, one experimental flaw radius was not properly estimated. Nevertheless, the depth estimations recorded a limited error of 0.75 mm. This leads to the conclusion that more accurate simulations would improve the ANN training procedure and consequently flaws radius and depths estimations when using experimental data.

The ultimate goal is to implement an ANN algorithm coupling different Non Destructive Testing methods. This could allow exploitation of the advantages of each technique and to properly detect and evaluate a large variety of flaws, overcoming the limitations due to the ECs skin effect.

Author statement

All authors certify that they have participated sufficiently in the work to take public responsibility for the content, including participation in the concept, design, analysis, writing, or revision of the manuscript.

Declaration of competing interest

The authors declare the following financial interests/personal relationships which may be considered as potential competing interests:

Acknowledgment

The authors would like to thank Matthieu FEUILLOY, Fabien CHHEL and Nicolas GUTOWSKI for their help and constructive comments. This research is funded by RFI-WISE, Pays de la Loire, France.

References

[1] Hellier C. Handbook of non destructive evaluation. McGraw-Hill Professional; 2001.
[2] Dumont-Fillon J. Contrôle non destructif. Techniques de l'Ingénieur 1996;1:1–42.
[3] Heideklang R, Shokouhi P. Application of data fusion in nondestructive testing (NDT). In: Proceedings of the 16th international conference on information fusion, FUSION 2013. IEEE; 2013. p. 835–41.
[4] He Y, Gao B, Sophian A, Yang R. In: Transient electromagnetic-thermal nondestructive testing. first ed. edition. Elsevier; 2017.
[5] Ravat C. Conception de multicapteurs à courants de Foucault et inversion des signaux associés pour le contrôle non destructif, phdthesis. Université Paris Sud-Paris 2008;XI.
[6] Sabbagh HA, Murphy RK, Sabbagh EH, Aldrin JC, Knopp JS. Computational electromagnetics and model-based inversion, scientific computation. New York: Springer; 2013.
[7] Klein G, Morelli J, Krause T. Evaluation of effect of temperature variation on pressure tube to calandria tube gap measurements. In: Our nuclear future: renewal and responsibility 37th Annual CNS conference and 41st CNS/CNA student conference, vol. 50; 2017. p. 617–24.
[8] Tian GY, Sophian A. Defect classification using a new feature for pulsed eddy current sensors. NDT E Int 2005;38:77–82.
[9] Buck JA, Underhill PR, Morelli JE, Krause TW. Simultaneous multiparameter measurement in pulsed eddy current steam generator data using artificial neural networks. IEEE Trans Instrum Meas 2016;65:672–9.
[10] Nikhil J. The rebirth of eddy current nondestructive testing: advanced techniques such as ACFM and Eddy Current Array are making rapid strides. Quality 2014;53: S19+.
[11] Stoll RL. The analysis of Eddy currents, monographs in electrical and electronic engineering. Clarendon Press; 1974.
[12] Pavo J, Lesselier D. Calculation of eddy current testing probe signal with global approximation. IEEE Trans Magn 2006;42:1419–22.
[13] Clauzon T, Thollon F, Nicolas A. Flaws characterization with pulsed eddy currents NDT. IEEE Trans Magn 1999;35:1873–6.
[14] Tamburrino A, Vento A, Ventre S, Maffucci A. Monotonicity imaging method for flaw detection in aeronautical applications. Stud Appl Electromagn Mech 2016;41: 284–92.
[15] Wang GG, Shan S. Review of metamodeling techniques in support of engineering design optimization. J Mech Des, Trans ASME 2007;129:370–80.
[16] Bilicz S, Lambert M, Gyimothy S, Pavo J. Solution of inverse problems in nondestructive testing by a kriging-based surrogate model. IEEE Trans Magn 2012; 48:495–8.
[17] Aldrin JC, Oneida EK, Shell EB, Sabbagh HA, Sabbagh E, Murphy RK, Mazdiyasni S, Lindgren EA, Mooers RD. Model-based probe state estimation and crack inverse methods addressing eddy current probe variability. In: AIP conference proceedings, vol. 1806; 2017.
[18] Shell EB, Aldrin JC, Sabbagh HA, Sabbagh E, Murphy RK, Mazdiyasni S, Lindgren EA. Demonstration of model-based inversion of electromagnetic signals for crack characterization. In: AIP conference proceedings, vol. 1650; 2015. p. 484–93.
[19] Oneida EK, Shell EB, Aldrin JC, Sabbagh HA, Sabbagh EH, Murphy RK, Mazdiyasni S, Lindgren EA. Flaw characterization using inversion of eddy current response and the effect of filters and scan resolution. In: AIP conference proceedings, vol. 1706; 2016.
[20] Bernieri A, Ferrigno L, Laracca M, Molinara M. Crack shape reconstruction in Eddy current testing using machine learning systems for regression. IEEE Trans Instrum Meas 2008;57:1958–68.
[21] Salucci M, Anselmi N, Oliveri G, Calmon P, Miorelli R, Reboud C, Massa A. Real-time NDT-NDE through an innovative adaptive partial least squares SVR inversion approach. IEEE Trans Geosci Rem Sens 2016;54:6818–32.
[22] Ahmed S, Miorelli R, Calmon P, Anselmi N, Salucci M. Real time flaw detection and characterization in tube through partial least squares and SVR: application to eddy current testing. In: AIP conference proceedings, vol. 1949; 2018.
[23] Ahmed S, Reboud C, Lhuillier PE, Calmon P, Miorelli R. An adaptive sampling strategy for quasi real time crack characterization on eddy current testing signals. NDT E Int 2019;103:154–65.
[24] Massa A, Boni A, Donelli M. A classification approach based on SVM for electromagnetic subsurface sensing. IEEE Trans Geosci Rem Sens 2005;43: 2084–93.
[25] Bermani E, Boni A, Caorsi S, Massa A. An innovative real-time technique for buried object detection. IEEE Trans Geosci Rem Sens 2003;41:927–31.
[26] Udpa L, Udpa SS. Application of neural networks for classification of eddy current NDT data. In: Review of progress in quantitative nondestructive evaluation. Boston, MA: Springer US; 1990. p. 673–80.
[27] Caorsi S, Gamba P. Electromagnetic detection of dielectric cylinders by a neural network approach. IEEE Trans Geosci Rem Sens 1999;37:820–7.
[28] Bihan YL, Pavo J, Marchand C. Characterization of small cracks in eddy current testing. Eur Phys J Appl Phys 2008;43:231–7.
[29] Babaei A, Suratgar AA, Salemi AH. Dimension estimation of rectangular cracks using impedance changes of the eddy current probe with a neural network. J Appl Res Technol 2013;11:397–401.
[30] Helifa B, Féliachi M, Lefkaier IK, Boubenider F, Zaoui A, Lagraa N. Characterization of surface cracks using eddy current NDT simulation by 3D-FEM and inversion by neural network. Appl Comput Electromagn Soc J 2016;31:187–94.
[31] Harzallah S, Rebhi R, Chabaat M, Rabehi A. Eddy current modelling using multi-layer perceptron neural networks for detecting surface cracks. Frat Ed Integrità Strutt 2018;12:147–55.
[32] Dai L, Feng H, Wang T, Xuan W, Liang Z, Yang X. Pipe crack recognition based on eddy current NDT and 2D impedance characteristics. Appl Sci 2019;9.
[33] Zhu P, Cheng Y, Banerjee P, Tamburrino A, Deng Y. A novel machine learning model for eddy current testing with uncertainty. NDT E Int 2019;101:104–12.
[34] LeCun Y. Connectionist Learning Models, Intellectica, special issue apprentissage et machine. 1987.
[35] Hagan MT, Demuth HB, Beale MH. Neural network design. Boston Massachusetts PWS 1995;2:734.
[36] Bishop CM. Pattern recognition and machine learning. Springer; 2006.
[37] Rosado LS, Janeiro FM, Ramos PM, Piedade M. Defect characterization with eddy current testing using nonlinear-regression feature extraction and artificial neural networks. IEEE Trans Instrum Meas 2013;62:1207–14.
[38] Bengio Y. Learning deep architectures for AI. Foundations and Trends® in Machine Learning 2009;2:1–127.
[39] Viana FAC, Venter G, Balabanov V. An algorithm for fast optimal Latin hypercube design of experiments. International 2009;82:135–56.
[40] Crombecq K, Laermans E, Dhaene T. Efficient space-filling and non-collapsing sequential design strategies for simulation-based modeling. Eur J Oper Res 2011; 214:683–96.
[41] Ana Alonso Rodríguez AV. Eddy current approximation of maxwell equations: theory, algorithms and applications, vol. 4. Springer Milan; 2010.
[42] Henneron T. Contribution à la prise en compte des Grandeurs Globales dans les Problèmes d'Electromagnétisme résolus avec la Méthode des Eléments Finis, phdthesis. Université Lille1 - Sciences et Technologies; 2004.
[43] Marquardt DW. An algorithm for least-squares estimation of nonlinear parameters. J Soc Ind Appl Math 1963;11:431–41.
[44] Jolliffe IT. Principal component analysis, springer series in Statistics. New York: Springer-Verlag; 2002.
[45] Sophian A, Tian GY, Taylor D, Rudlin J. A feature extraction technique based on principal component analysis for pulsed Eddy current NDT. NDT E Int 2003;36: 37–41.
[46] Akima H. A new method of interpolation and smooth curve fitting based on local procedures. J ACM 1970;17:589–602.
[47] Amidror I. Scattered data interpolation methods for electronic imaging systems: a survey. J Electron Imag 2002;11:157.
[48] Lehmann EL, Casella G. In: Theory of point estimation. second ed. New York, NY, USA: Springer-Verlag; 1998.
[49] Hagan MT, Menhaj MB. Training feedforward networks with the marquardt algorithm. IEEE Trans Neural Network 1994;5:989–93.